Editors' Suggestion | Featured in Physics

Experimental Observation of Hidden Multistability in Nonlinear Systems

Kun Zhang,* Qicheng Zhang,* Shuaishuai Tong, Wenquan Wu, Xiling Feng, and Chunyin Qiu†
Key Laboratory of Artificial Micro- and Nano-Structures of Ministry of Education and School of Physics and Technology, Wuhan University, Wuhan 430072, China

(Received 18 February 2025; revised 21 September 2025; accepted 25 November 2025; published 20 January 2026)

Multistability—the coexistence of multiple stable states—is a cornerstone of nonlinear dynamical systems, governing their equilibrium, tunability, and emergent complexity. Recently, the concept of hidden multistability, where certain stable states evade detection via conventional continuous parameter sweeping, has garnered increasing attention due to its elusive nature and promising applications. In this Letter, we present the first experimental observation of hidden multistability using a programmable acoustic coupled-cavity platform that integrates competing self-focusing and self-defocusing Kerr nonlinearities. Beyond established bistability, we demonstrate semihidden and fully hidden tristabilities by precisely programming system parameters. Crucially, the hidden stable states, typically inaccessible via the traditional protocol, are unambiguously revealed and dynamically controlled through pulsed excitation, enabling flexible transitions between distinct types of stable states. These experimental findings not only offer new insights into the fundamental physics of emerging hidden multistability, but also unlock new avenues for applications in information storage, information encryption, and safety precaution, where multistate dynamics could enable advanced control techniques.

DOI: 10.1103/5b5b-gnjw

Introduction—Nonlinearity plays a crucial role in shaping the complex behaviors of dynamical systems, giving rise to intricate phenomena such as chaos, solitons, and multistability. These phenomena, in turn, advance cutting-edge technologies and enhance fundamental understanding of natural processes [1]. In particular, the multistability refers to the coexistence of multiple stable states under a given set of parameters, with their emergence dependent on initial conditions. It has been observed across diverse scientific fields, including physics [2–10], chemistry [11,12], biology [13], neuroscience [14], ecology [15], genetics [16], and even climate science [17]. Typically, physical systems with multistability exhibit hysteresis under continuous parameter sweeping, and undergo transitions between different stable states due to random perturbations or deterministic controls. These properties make nonlinear systems particularly attractive for applications in information storage [18–21], switches [22–24], and logic gates [25–27].

Very recently, a fundamentally new class of multistability—hidden multistability—has been proposed theoretically [9]. Unlike the conventional multistability, it refers to the emergence of additional stable states that are folded within traditional hysteresis loops. As such, adiabatic parameter sweeping only guides the system along trajectories connecting explicit stable states [5], while leaving the embedded states hidden and unobservable. The existence of such hidden states could be a double-edged sword. On one hand, devices relying on known multistability may malfunction in real-world applications if random noise kicks the system into the hidden states [28–30]. On the other hand, such hidden states can securely store sensitive information, which makes unauthorized decryption exceedingly difficult without detailed system knowledge [31]. Therefore, identifying hidden multistability is crucial for understanding and regulating complex nonlinear systems. However, the experimental detection of hidden states, which are typically embedded in the system's hysteresis landscape, demands precise nonlinear control and a unique excitation strategy, which pose substantial challenges for current experimental platforms and technologies.

In this Letter, we present the first experimental evidence of hidden multistability using a programmable nonlinear acoustic platform. We start with a minimal yet representative driven-dissipative double-oscillator model that features both self-defocusing and self-focusing Kerr nonlinearities. By carefully balancing these nonlinearities, our model exhibits not only conventional bistability but also intricate semihidden and fully hidden tristabilities at different driving frequencies. To experimentally validate these phenomena—especially the elusive hidden multistabilities—we design and implement a coupled acoustic binary-cavity platform integrated with external circuits. In this setup, the long-sought acoustic Kerr nonlinearities, characterized by intensity-dependent blueshifts and redshifts of resonant frequencies, are elegantly realized via

*These authors contributed equally to this work.
†Contact author: cyqiu@whu.edu.cn

 © 2026 American Physical Society

active and programmable electroacoustic feedbacks—a key design to achieve precise nonlinear control. Under standard sound field sweeping, we observe a bistabilitylike hysteresis loop in the fully hidden tristability system—while the hidden states remain concealed and undetectable. Crucially, by employing an unusual pulsed excitation protocol, we successfully reveal the elusive hidden states and demonstrate controlled transitions among multiple stable states. Our findings, aligned well with those predicted from nonlinear coupled-mode theory, not only validate the existence of hidden multistability but also underscore the rich and intricate interplay among drive, dissipation, and nonlinearity.

Theoretical model with multistability and hidden states—As sketched in Fig. 1(a), we consider a nonlinear driven-dissipative double-oscillator model, where the oscillators, each with intrinsic loss γ_0, are coupled through reciprocal coupling g. The nonlinearity arises from the self-defocusing and self-focusing Kerr effects [32–35] of oscillators 1 and 2, respectively. It is characterized by the intensity-dependent resonant frequencies $\omega_1 = -\Delta\omega + k_1|\psi_1|^2$ and $\omega_2 = +\Delta\omega - k_2|\psi_2|^2$, where $\pm\Delta\omega$ are linear frequencies, $k_{1,2} > 0$ are nonlinear coefficients, and $\psi_{1,2}$ represent state components. A harmonic drive $D = A_d e^{-i\omega_d t}$ is applied to oscillator 2, with A_d and ω_d being the driving amplitude and frequency, respectively. The dynamics of this model is governed by the Gross-Pitaevskii equation

$$i\frac{d\Psi}{dt} = \begin{bmatrix} \omega_1 - i\gamma_0 & g \\ g & \omega_2 - i\gamma_0 \end{bmatrix}\Psi + \begin{bmatrix} 0 \\ 1 \end{bmatrix} D, \qquad (1)$$

where $\Psi = e^{-i\omega_d t}[\psi_1, \psi_2]^T$. To avoid strong nonlinear phenomena like limit cycles and chaos [36,37], we focus on the weakly nonlinear regime, where the static solutions take the form $\psi_{1,2} = A_{1,2}e^{-i\theta_{1,2}}$, with $A_{1,2}$ and $\theta_{1,2}$ representing the magnitudes and phases, respectively. More concretely, from Eq. (1) we obtain a higher-order equation for the intensity $I_1 = A_1^2$ of oscillator 1

$$[g^2 - 2(\Lambda_2 - k_2\Pi g^{-2}I_1)(\Lambda_1 + k_1 I_1) + 2\gamma_0^2 + \Pi g^{-2}\gamma_0^2 + \Pi g^{-2}(\Lambda_2 - k_2\Pi g^{-2}I_1)^2]I_1 - A_d^2 = 0, \qquad (2)$$

where $\Pi = (-\Delta\omega - \omega_d + k_1 I_1)^2 + \gamma_0^2$, $\Lambda_1 = -\Delta\omega - \omega_d$, and $\Lambda_2 = \Delta\omega - \omega_d$. Using the Routh-Hurwitz criterion, the meaningful solutions for $I_1 > 0$ can be classified into stable and unstable states of the system (see details in Supplemental Material [38]).

To facilitate our subsequent experiments, the model parameters are set to $\Delta\omega = 43$ Hz, $\gamma_0 = 13$ Hz, $g = 17.5$ Hz, $k_1 = 3.8$, and $k_2 = 1$. Figure 1(b) displays the phase diagram of stable states for $A_d \in [80, 200]$ and $\omega_d \in [-30, 0]$ Hz. Because of the complex interplay of drive, loss, and nonlinearity, the model can exhibit two or three coexisting stable states, depending on the driving parameters A_d and ω_d. Based on the magnitude of ψ_1, the stable states are labeled as lower state (LS), higher state (HS), and intermediate state (IS). Meanwhile, according to the overlap of stable states at a fixed ω_d, the phase diagram is divided into different regimes. These include bistability, where only LS and HS coexist within a range of A_d; fully hidden tristability, where an additional IS emerges within the LS-HS overlap range; and semihidden tristability, where IS partially extends beyond the overlap. Figure 1(c) exemplifies the three multistabilities under adiabatic sweeps of A_d. In the case of $\omega_d = -2$ Hz, as A_d increases, the system evolves along the LS path to a bifurcation point and then jumps up to HS; conversely, as A_d decreases, it follows the HS path to another bifurcation point and finally jumps down to LS. The forward and backward sweeps together form a characteristic hysteresis loop of bistability. Surprisingly, in the case of fully hidden tristability ($\omega_d = -12$ Hz), despite the presence of an additional IS,

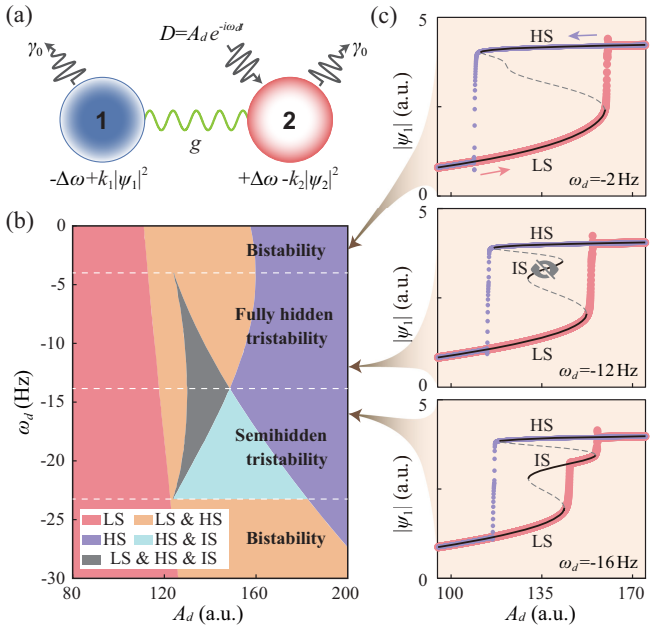

FIG. 1. Theoretical model. (a) Nonlinear driven-dissipative double-oscillator model. Here $\omega_1 = -\Delta\omega + k_1|\psi_1|^2$ and $\omega_2 = \Delta\omega - k_2|\psi_2|^2$ are intensity-dependent resonant frequencies of the two oscillators, γ_0 is intrinsic loss, g is the coupling between the oscillators, and $D = A_d e^{-i\omega_d t}$ characterizes the drive applied to oscillator 2. (b) Phase diagram. The model supports three stable states, dubbed lower state (LS), higher state (HS), and intermediate state (IS), under different driving amplitude A_d and frequency ω_d. According to the overlap of states at a fixed ω_d, the model exhibits bistability, fully hidden tristability, and semihidden tristability. (c) State evolutions under adiabatic sweeps of A_d, corresponding to bistability (top), fully hidden tristability (middle), and semihidden tristability (bottom). The black solid and gray dashed lines specify the stable and unstable states, respectively. The red and purple dots represent the numerical stable states during the forward and backward sweeps of A_d, respectively. The parameters used for the calculations are $\Delta\omega = 43$ Hz, $\gamma_0 = 13$ Hz, $g = 17.5$ Hz, $k_1 = 3.8$, and $k_2 = 1$.

the system exhibits similar hysteresis that renders the IS completely hidden. In semihidden tristability ($\omega_d = -16$ Hz), the system transitions from LS to IS and subsequently to HS during a forward A_d sweep, in contrast to the direct transition from HS to LS under a backward sweep. This leads to a partially observable IS, while the remainder is hidden within the LS-HS overlap.

Here, we emphasize that multistability in nonlinear systems is typically highly sensitive to both intrinsic and external parameters. As exemplified by our model [Fig. 1(b)], even a slight shift in the driving frequency can steer the system into entirely different multistable regimes. This pronounced sensitivity carries two crucial implications: on the one hand, it may result in unanticipated outcomes in laboratory experiments or real-world applications; on the other hand, it imposes stringent demands on experimental setups—necessitating precise control over system parameters and accurate measurements to reliably identify hidden multistability.

Experimental implementation of a nonlinear acoustic platform—To realize the theoretical model introduced above, we construct an acoustic coupled binary-cavity system with balanced self-focusing and self-defocusing Kerr nonlinearities. Remarkably, while acoustic coupled-cavity systems have been widely employed in exploring (linear) topological and non-Hermitian physics [39–48], those incorporating nonlinear effects have yet to be realized. As depicted in Fig. 2(a), the air-filled cavities 1 and 2 feature intrinsic dipole resonant frequencies of 3954 and 4040 Hz, respectively, yielding a central reference frequency $\omega_o = 3997$ Hz and the desired $\Delta\omega = 43$ Hz for the system. Reciprocal acoustic coupling, $g = 17.5$ Hz, is generated via two narrow tubes connecting the cavities. The cavity losses γ_0, originally 35 Hz, are compensated to 13 Hz using two linear electroacoustic self-gain modules [43–48], each consisting of a microphone, a preamplifier, a phase shifter, and a speaker [Fig. 2(a), top]. (Notably, the phase shifter provides additional flexibility to compensate for the phase shift introduced by the circuits [46], thereby maintaining the original resonant frequency of the cavity.) Unlike the Kerr-type nonlinearities inherent in optical media or cavity magnonic systems [49–53], airborne sound waves generally exhibit weak nonlinearities that cannot be readily harnessed. Here, we realize acoustic Kerr nonlinearities by ingeniously introducing two nonlinear electroacoustic feedback modules [Fig. 2(a), bottom]. In each module, the sound signal within a cavity is collected by a microphone, modulated by a preamplifier, voltage-controlled amplifier, and phase shifter, and then fed back into the cavity via a speaker. Meanwhile, the gain factor of the voltage-controlled amplifier is dynamically adjusted by a microcomputer, which is custom-coded to respond to the preamplified signal (proportional to sound pressure in the cavity). Ultimately, our electroacoustic feedback-assisted experimental platform offers exceptional programmability,

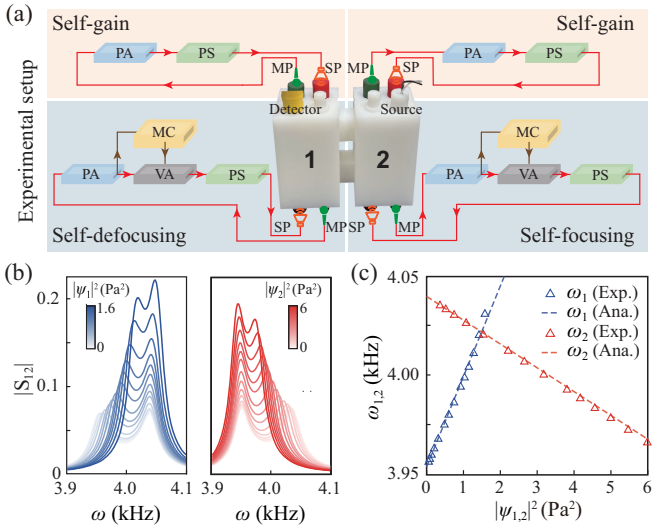

FIG. 2. Nonlinear acoustic coupled binary-cavity system. (a) Experimental setup. Two air-filled acoustic cavities act as oscillators, with narrow tubes between them producing reciprocal coupling. To tune cavity losses, two linear electroacoustic self-gain modules (top) are employed, each comprising microphone (MP), preamplifier (PA), phase shifter (PS), and speaker (SP). To generate self-defocusing and self-focusing nonlinearities, two nonlinear electroacoustic feedback modules (bottom) are introduced, each consisting of MP, PA, voltage-controlled amplifier (VA), PS, microcomputer (MC) and SP. (b) Sound intensity-dependent transmission spectra $|S_{12}|$, in which the nonlinear modules are individually implemented to cavities 1 (left) and 2 (right), through which one can extract their resonant frequencies. (c) Quantitative relations between the resonant frequencies and sound intensities. The linearly shaped blueshift of ω_1 with $|\psi_1|^2$ and redshift of ω_2 with $|\psi_2|^2$ indicate the presence of self-defocusing and self-focusing Kerr nonlinearities in cavities 1 and 2, respectively.

providing precise parameter control for probing and manipulating complex nonlinear dynamics.

With nonlinear modules individually applied to cavities 1 and 2, we measured the transmission spectra $|S_{12}|$—the response amplitude of cavity 1 to a source in cavity 2—under varying sound intensities $|\psi_1|^2$ and $|\psi_2|^2$. By numerically fitting the spectra [Fig. 2(b)] with the established coupled-mode theory [54,55], we extracted the resonant frequencies of the two cavities [Fig. 2(c)]. As required by our preset parameters ($\Delta\omega = 43$ Hz, $k_1 = 3.8$, and $k_2 = 1$), the data follow the quantitative relations $\omega_1 \approx \omega_o + (-43 + 3.8l|\psi_1|^2)$ Hz and $\omega_2 \approx \omega_o + (43 - l|\psi_2|^2)$ Hz. (Note that the shift of central frequency to ω_o and the scaling factor $l = 12$ do not affect the essential physics of the system.) Specifically, when the nonlinear module in cavity 1 operates independently, ω_1 exhibits a blueshift with increasing $|\psi_1|^2$, indicating the desired self-defocusing nonlinearity in cavity 1. In contrast, when the nonlinear module in cavity 2 is active, ω_2 undergoes a redshift as $|\psi_2|^2$ increases, suggesting the expected self-focusing nonlinearity

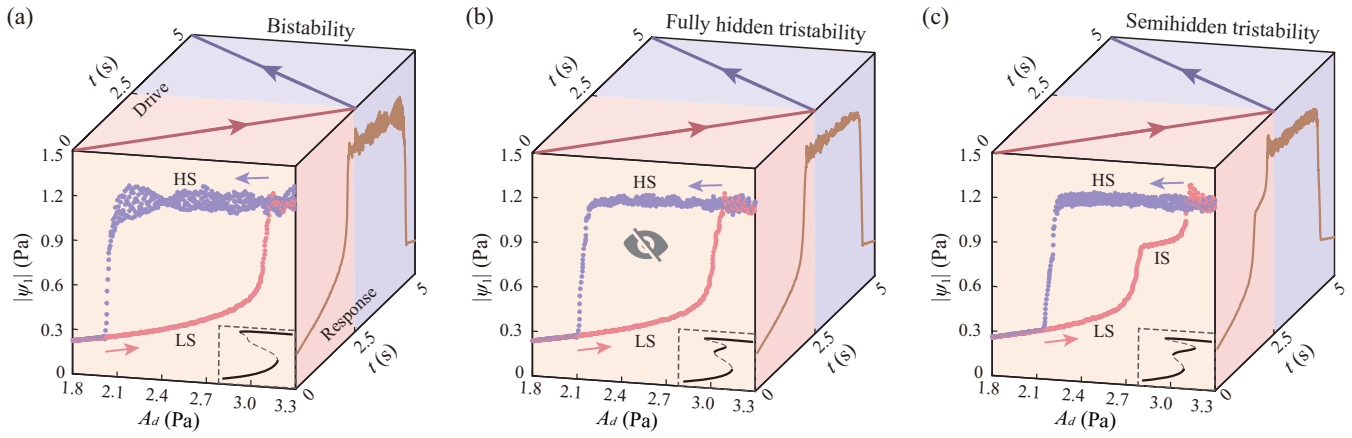

FIG. 3. Experimental characterization of hysteresis loops under continuous sound sweeping. (a)–(c) Hysteresis loops measured for bistability, fully hidden tristability, and semihidden tristability, where the driving frequencies are 3995, 3985, and 3981 Hz, respectively. In each cube, the top surface illustrates the temporal variation of driving sound pressure in cavity 2, the side surface displays the sound pressure response in cavity 1, and the front surface shows the state evolutions under sound sweeping. Insets: theoretically predicted multistabilities. In comparison to the partially observed IS in semihidden tristability, the IS cannot be detected through sound sweeping in fully hidden tristability.

in cavity 2. Notably, although the absolute frequency shift is measured on an Hz scale, its relative value with respect to the operating frequency (ω_o) reflects a controllable nonlinear strength comparable to that observed in other systems, such as the magnonic system discussed in Ref. [5]. More experimental details are provided in Supplemental Material [38].

Experimental evidence of multistability and hidden states—We first demonstrate the hysteresis loops of multistabilities in our system through continuous sound pressure sweeping. To achieve the bistability predicted in Fig. 1(c), we drive the system from cavity 2 at a monochromatic sound of 3995 Hz (equivalent to $\omega_d = -2$ Hz in our theoretical model, with the central reference frequency $\omega_o = 3997$ Hz). The pressure amplitude A_d is continuously increased and decreased during the forward and backward sweeps, each of which lasts 2.5 s [Fig. 3(a), top surface]. (For experimental feasibility, we choose a total measurement duration of $t = 5$ s, allowing us to reliably track the state evolution without compromising adiabaticity). To monitor the state evolution, we measure the sound pressure response $|\psi_1|$ in cavity 1 [Fig. 3(a), side surface]. By combining the drive-response data, we observe a hysteresis loop of bistability in the $A_d - |\psi_1|$ plane [Fig. 3(a), front surface]. During the forward sweep, as A_d linearly increases from 1.80 to 3.30 Pa, the system evolves gradually along the LS and undergoes a sharp transition to the HS at $A_d \approx 3.05$ Pa, after which the system stabilizes at the HS. Conversely, during the backward sweep, the system remains in the HS until A_d decreases to 2.10 Pa, at which it abruptly switches back to the LS. Remarkably, when the driving frequency is tuned to 3985 Hz (equivalently, $\omega_d = -12$ Hz), $|\psi_1|$ traces a characteristic hysteresis loop similar to that of bistability [Fig. 3(b)]. That is, despite the expectation of tristability (see inset), we are unable to reach the theoretically predicted IS in both the forward and backward parameter sweeps. This underscores the nature of the hidden multistability. Further lowering the driving frequency to 3981 Hz (equivalently, $\omega_d = -16$ Hz), the system exhibits a more complex hysteresis structure of multistability [Fig. 3(c)]. During the forward sweep, $|\psi_1|$ undergoes two abrupt jumps at $A_d \approx 2.71$ Pa and 3.07 Pa, transitioning from LS to IS and from IS to HS, respectively. Conversely, in the backward sweep, the system directly evolves from HS to LS, where the predicted hidden states in this semihidden tristability, as expected, are not detected again.

Next, we experimentally reveal the hidden states and fully hidden tristability by employing an unusual sound pulsing excitation. According to the results in Fig. 3(b), we first drive the system with a sound signal of 3985 Hz and $A_d = 2.68$ Pa to initiate an LS with $|\psi_1| \approx 0.43$ Pa, as shown in Fig. 4(a). At $t = 150$ ms, we apply a positive sound pulse with a height of 0.92 pa and a duration of 20 ms. This induces a rapid increase in $|\psi_1|$ and pushes the system into the attraction basin of IS. After the driving signal is restored ($t > 170$ ms), $|\psi_1|$ continues to rise and eventually settles at 0.96 Pa—this final value clearly indicates that the system has landed on the hidden IS. Note that both the duration and amplitude of the pulse are crucial for the transition LS → IS. A pulse that is too short (weak) cannot excite the LS into the IS basin, eventually causing the system to return to the LS. Conversely, a pulse that is too long (strong) will drive the system into the attraction basin of HS. For example, as shown in Fig. 4(a), when we extend the pulse duration to 50 ms, the system bypasses the IS basin and directly falls into the HS with $|\psi_1| \approx 1.23$ Pa. (The oscillation of $|\psi_1|$ at the HS can be attributed to the instability of the experimental system

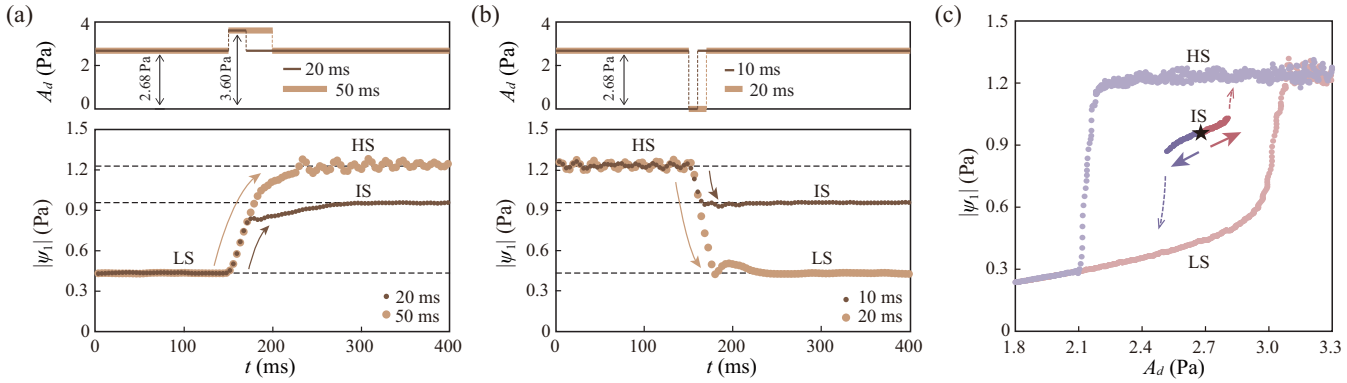

FIG. 4. Experimental observation of hidden states and fully hidden tristability. (a) Positive sound pulses (top) and the resultant transitions from LS to IS and HS (bottom). A hidden IS is excited from the LS by a positive pulse of 0.92 Pa in height and 20 ms in duration (dark brown), while an HS is converted from the LS by a longer positive pulse of 50 ms duration (light brown). (b) Negative sound pulses (top) and the resultant transitions from HS to IS and LS. As expected, a short negative pulse transitions the HS to a hidden IS, while a long negative pulse switches it to LS. (c) Unveiling of fully hidden tristability. The complete IS is detected through forward and backward sound sweeps (dark colored), starting from the hidden IS (star) detected in (a). For comparison, the hysteresis loop from Fig. 3(b) is also displayed (light colored).

under relatively strong nonlinearity.) Similarly, we can induce the transitions from HS to the hidden IS and LS through applying negative pulses. As shown in Fig. 4(b), starting from a HS of $|\psi_1| \approx 1.23$ Pa, a negative pulse with a depth of 2.68 Pa and a duration of 10 ms drives the system to the hidden IS, while a longer 20 ms pulse transitions the system directly to the LS. More experimental results can be seen in Supplemental Material [38]. It is worth noting that only a single hidden IS is detected in each sound pulsing excitation. To construct the complete hidden IS path embedded within the hysteresis loop, we further perform forward and backward sound field sweeps, starting from a known hidden IS. As shown in Fig. 4(c), the entire hidden IS within the range of $A_d \in [2.52, 2.81]$ Pa is revealed around the single hidden IS at $A_d = 2.68$ Pa. Combined with the hysteresis loop obtained in Fig. 3(b), now all three stable states of the fully hidden tristability are clearly identified in our experiments. Similar treatment can be applied to the system of semihidden tristability, where the hidden states missed in Fig. 3(c) can be uncovered as expected (see Supplemental Material [38]).

Conclusions and outlook—We have experimentally identified the presence of hidden multistability, a subtle and previously unobserved nonlinear phenomenon, using our newly developed nonlinear acoustic platform. Beyond the hysteresis loops uncovered via standard sound field sweeping, the elusive hidden states (and their transitions from known stable states) are explicitly revealed and dynamically controlled via unusual pulse excitation protocol. Our Letter not only brings the study of hidden multistability to the experimental level, but also inspires innovative control of multistate dynamics in nonlinear systems across a broad spectrum of scientific fields, including optics, mechanics, magnonics, electronic circuits, and even neuroscience and ecology.

Looking ahead, our nonlinear acoustic platform offers exciting opportunities for uncovering even more complex multistable configurations, such as hierarchical hidden states, through the introduction of additional coupled cavities or drives. Its high programmability, powered by electroacoustic feedback modules, permits precise and flexible control over on-site frequencies, gain and loss distributions, and reciprocal and nonreciprocal couplings as functions of sound intensity, time, and other parameters. The resultant scalability facilitates the further integration of diverse advanced physical effects—including non-Hermiticity, synthetic gauge fields, band topology, and spatiotemporal modulations—making our experimental platform a versatile tool for exploring their rich interplay with nonlinear dynamics. Owing to the universal nature of these physical effects across different systems, our Letter not only establishes a foundation for developing intelligent multifunctional acoustic metamaterials, but also paves the way for exploring a wide spectrum of cutting-edge physical phenomena beyond acoustics, including nonlinear bulk-edge correspondence [56–60], nonlinear topological solitons [50,51,61–63], nonlinear Thouless pumping [64–67], nonlinear skin effects [35,68–72], and nonlinear exceptional points [73,74].

Note added—We recently became aware of a related study reporting anomalous state transitions and complete multistate excitation induced by nonlinear acoustic coupling [75].

Acknowledgments—This work was supported by the National Natural Science Foundation of China (Grants No. 12374418, No. 12104346, and No. 12304495), the Natural Science Foundation of Hubei Province of China (No. 2024AFB654), and the Fundamental Research Funds

for the Central Universities, and the National Key R&D Program of China (Grant No. 2023YFA1406900).

Data availability—The data that support the findings of this Letter are not publicly available upon publication because it is not technically feasible and/or the cost of preparing, depositing, and hosting the data would be prohibitive within the terms of this research project. The data are available from the authors upon reasonable request.

[1] S. H. Strogatz, *Nonlinear Dynamics and Chaos: With Applications to Physics, Biology, Chemistry, and Engineering* (Westview Press, Boulder, CO, USA, 2015).

[2] V. Kubytskyi, S.-A. Biehs, and P. Ben-Abdallah, Radiative bistability and thermal memory, Phys. Rev. Lett. **113**, 074301 (2014).

[3] H. Yasuda and J. Yang, Reentrant origami-based metamaterials with negative Poisson's ratio and bistability, Phys. Rev. Lett. **114**, 185502 (2015).

[4] F. Letscher, O. Thomas, T. Niederprüm, M. Fleischhauer, and H. Ott, Bistability versus metastability in driven dissipative Rydberg gases, Phys. Rev. X **7**, 021020 (2017).

[5] Y.-P. Wang, G.-Q. Zhang, D. Zhang, T.-F. Li, C.-M. Hu, and J. Q. You, Bistability of cavity magnon polaritons, Phys. Rev. Lett. **120**, 057202 (2018).

[6] H. B. Chan, V. A. Aksyuk, R. N. Kleiman, D. J. Bishop, and F. Capasso, Nonlinear micromechanical Casimir oscillator, Phys. Rev. Lett. **87**, 211801 (2001).

[7] M. X. Bi, X. H. Yan, Y. Zhang, and Y. Xiao, Tristability of cavity magnon polaritons, Phys. Rev. B **103**, 104411 (2021).

[8] R.-C. Shen, J. Li, Z.-Y. Fan, Y.-P. Wang, and J. Q. You, Mechanical bistability in Kerr-modified cavity magnomechanics, Phys. Rev. Lett. **129**, 123601 (2022).

[9] M.-X. Bi, H. Fan, X.-H. Yan, and Y.-C. Lai, Folding state within a hysteresis loop: Hidden multistability in nonlinear physical systems, Phys. Rev. Lett. **132**, 137201 (2024).

[10] Skripka, Z. Zhang, X. Qi, B. Ursprung, P. Ercius, B. E. Cohen, P. J. Schuck, D. Jaque, and E. M. Chan, Intrinsic optical bistability of photon avalanching nanocrystals, Nat. Photonics **19**, 212 (2025).

[11] C. Simáo, M. Mas-Torrent, N. Crivillers, V. Lloveras, J. M. Artés, P. Gorostiza, J. Veciana, and C. Rovira, A robust molecular platform for non-volatile memory devices with optical and magnetic responses, Nat. Chem. **3**, 359 (2011).

[12] S. N. Semenov, L. J. Kraft, A. Ainla, M. Zhao, M. Baghbanzadeh, V. E. Campbell, K. Kang, J. M. Fox, and G. M. Whitesides, Autocatalytic, bistable, oscillatory networks of biologically relevant organic reactions, Nature (London) **537**, 656 (2016).

[13] D. R. Burrill and P. A. Silver, Making cellular memories, Cell **140**, 13 (2010).

[14] J. Brascamp, R. Blake, and T. Knapen, Negligible fronto-parietal BOLD activity accompanying unreportable switches in bistable perception, Nat. Neurosci. **18**, 1672 (2015).

[15] M. Hirota, M. Holmgren, E. H. Van Nes, and M. Scheffer, Global resilience of tropical forest and savanna to critical transitions, Science **334**, 232 (2011).

[16] T. S. Gardner, C. R. Cantor, and J. J. Collins, Construction of a genetic toggle switch in Escherichia coli, Nature (London) **403**, 339 (2000).

[17] A. L. Zerkle, M. W. Claire, S. D. Domagal-Goldman, J. Farquhar, and S. W. Poulton, A bistable organic-rich atmosphere on the Neoarchaean Earth, Nat. Geosci. **5**, 359 (2012).

[18] T. Tanabe, M. Notomi, S. Mitsugi, A. Shinya, and E. Kuramochi, Fast bistable all-optical switch and memory on a silicon photonic crystal on-chip, Opt. Lett. **30**, 2575 (2005).

[19] R. Fermin, N. M. A. Scheinowitz, J. Aarts, and K. Lahabi, Mesoscopic superconducting memory based on bistable magnetic textures, Phys. Rev. Res. **4**, 033136 (2022).

[20] A. A. Nikitin, I. A. Ryabcev, A. A. Nikitin, A. V. Kondrashov, A. A. Semenov, D. A. Konkin, A. A. Kokolov, F. I. Sheyerman, L. I. Babak, and A. B. Ustinov, Optical bistable SOI micro-ring resonators for memory applications, Opt. Commun. **511**, 127929 (2022).

[21] J.-S. Kim, C.-S. Ri, Y.-J. Yun, S.-J. Im, K.-D. Kim, K.-S. Song, J.-S. Pae, and K.-S. Ho, On-chip deep subwavelength optomagnetic bistable memory based on inverse Faraday effect related nonlinearity in graphene waveguide ring resonators, Phys. Rev. B **110**, 195421 (2024).

[22] E. G. Emberly and G. Kirczenow, The smallest molecular switch, Phys. Rev. Lett. **91**, 188301 (2003).

[23] M. F. Yanik, S. Fan, M. Soljačić, and J. D. Joannopoulos, All-optical transistor action with bistable switching in a photonic crystal cross-waveguide geometry, Opt. Lett. **28**, 2506 (2003).

[24] B. T. Worrell, M. K. McBride, G. B. Lyon, L. M. Cox, C. Wang, S. Mavila, C.-H. Lim, H. M. Coley, C. B. Musgrave, Y. Ding, and C. N. Bowman, Bistable and photoswitchable states of matter, Nat. Commun. **9**, 2804 (2018).

[25] Y. Tadokoro and H. Tanaka, Highly sensitive implementation of logic gates with a nonlinear nanomechanical resonator, Phys. Rev. Appl. **15**, 024058 (2021).

[26] R.-C. Shen, Y.-P. Wang, J. Li, S.-Y. Zhu, G. S. Agarwal, and J. Q. You, Long-time memory and ternary logic gate using a multistable cavity magnonic system, Phys. Rev. Lett. **127**, 183202 (2021).

[27] N. Yang, Y. Lan, M. Zhao, X. Shi, K. Huang, Z. Mao, and D. Padovani, Bistable soft shells for programmable mechanical logic, Adv. Sci. **12**, 2412372 (2025).

[28] C. Stambaugh and H. B. Chan, Noise-activated switching in a driven nonlinear micromechanical oscillator, Phys. Rev. B **73**, 172302 (2006).

[29] J. M. Newby and M. A. Schwemmer, Effects of moderate noise on a limit cycle oscillator: Counterrotation and bistability, Phys. Rev. Lett. **112**, 114101 (2014).

[30] V. V. Semenov, A. B. Neiman, T. E. Vadivasova, and V. S. Anishchenko, Noise-induced transitions in a double-well oscillator with nonlinear dissipation, Phys. Rev. E **93**, 052210 (2016).

[31] M. Borah and B. K. Roy, Hidden multistability in four fractional-order memristive, meminductive and memcapacitive chaotic systems with bursting and boosting phenomena, Eur. Phys. J. Special Topics **230**, 1773 (2021).

[32] Y. Zhang, Z. Chen, B. Wu, T. Busch, and V. V. Konotop, Asymmetric loop spectra and unbroken phase protection due to nonlinearities in PT-symmetric periodic potentials, Phys. Rev. Lett. **127**, 034101 (2021).
[33] C. Li and Y. V. Kartashov, Stable vortex solitons sustained by localized gain in a cubic medium, Phys. Rev. Lett. **132**, 213802 (2024).
[34] G. H. Alharbi, S. Wong, Y. Gong, and S. S. Oh, Asymmetrical temporal dynamics of edge modes in Su-Schrieffer-Heeger lattice with Kerr nonlinearity, Phys. Rev. Res. **6**, L042013 (2024).
[35] B. Many Manda, R. Carretero-González, P. G. Kevrekidis, and V. Achilleos, Skin modes in a nonlinear Hatano-Nelson model, Phys. Rev. B **109**, 094308 (2024).
[36] R. M. May, Simple mathematical models with very complicated dynamics, Nature (London) **261**, 459 (1976).
[37] K. Sone, M. Ezawa, Z. Gong, T. Sawada, N. Yoshioka, and T. Sagawa, Transition from the topological to the chaotic in the nonlinear Su-Schrieffer-Heeger model, Nat. Commun. **16**, 422 (2025).
[38] See Supplemental Material at http://link.aps.org/supplemental/10.1103/5b5b-gnjw for more theoretical and experimental details.
[39] H. Xue, Y. Yang, F. Gao, Y. Chong, and B. Zhang, Acoustic higher-order topological insulator on a kagome lattice, Nat. Mater. **18**, 108 (2019).
[40] Y. Qi, C. Qiu, M. Xiao, H. He, M. Ke, and Z. Liu, Acoustic realization of quadrupole topological insulators, Phys. Rev. Lett. **124**, 206601 (2020).
[41] H. Qiu, Q. Zhang, T. Liu, X. Fan, F. Zhang, and C. Qiu, Minimal non-Abelian nodal braiding in ideal metamaterials, Nat. Commun. **14**, 1261 (2023).
[42] Q. Zhang, Y. Leng, L. Xiong, Y. Li, K. Zhang, L. Qi, and C. Qiu, Construction and observation of flexibly controllable high-dimensional non-Hermitian skin effects, Adv. Mater. **36**, 2403108 (2024).
[43] L. Zhang, Y. Yang, Y. Ge, Y.-J. Guan, Q. Chen, Q. Yan, F. Chen, R. Xi, Y. Li, D. Jia, S.-Q. Y, H.-X. Sun, H. Chen, and B. Zhang, Acoustic non-Hermitian skin effect from twisted winding topology, Nat. Commun. **12**, 6297 (2021).
[44] J.-J. Liu, Z.-W. Li, Z.-G. Chen, W. Tang, B. Liang, G. Ma, and J.-C. Cheng, Experimental realization of Weyl exceptional rings in a synthetic three-dimensional non-Hermitian phononic crystal, Phys. Rev. Lett. **129**, 084301 (2022).
[45] Q. Zhang, Y. Li, H. Sun, X. Liu, L. Zhao, X. Feng, X. Fan, and C. Qiu, Observation of acoustic non-Hermitian Bloch braids and associated topological phase transitions, Phys. Rev. Lett. **130**, 017201 (2023).
[46] Z.-X. Chen, L.-L. Ma, S.-J. Ge, Z.-G. Chen, M.-H. Lu, Y.-F. Chen, and Y.-Q. Lu, Transient logic operations in acoustics through dynamic modulation, Phys. Rev. Appl. **21**, L011001 (2024).
[47] S. Tong, Q. Zhang, L. Qi, G. Li, X. Feng, and C. Qiu, Observation of Floquet-Bloch braids in non-Hermitian spatiotemporal lattices, Phys. Rev. Lett. **134**, 126603 (2025).
[48] S. Tong, Q. Zhang, G. Li, K. Zhang, C. Xie, and C. Qiu, Observation of momentum-band topology in PT-symmetric Floquet lattices, Nat. Commun. **16**, 9975 (2025).
[49] M. Segev, B. Crosignani, A. Yariv, and B. Fischer, Spatial solitons in photorefractive media, Phys. Rev. Lett. **68**, 923 (1992).
[50] Y. Lumer, Y. Plotnik, M. C. Rechtsman, and M. Segev, Self-localized states in photonic topological insulators, Phys. Rev. Lett. **111**, 243905 (2013).
[51] S. Mukherjee and M. C. Rechtsman, Observation of Floquet solitons in a topological bandgap, Science **368**, 856 (2020).
[52] J. L. Erskine and E. A. Stern, Magneto-optic Kerr effect in Ni, Co, and Fe, Phys. Rev. Lett. **30**, 1329 (1973).
[53] U. Tiwari, R. Ghosh, and P. Sen, Theory of magneto-optic Kerr effects, Phys. Rev. B **49**, 2159 (1994).
[54] H. A. Haus, *Waves and Fields in Optoelectronics* (Prentice-Hall, Englewood Cliffs, NJ, 1984).
[55] W. Suh, Z. Wang, and S. Fan, Temporal coupled-mode theory and the presence of non-orthogonal modes in lossless multimode cavities, IEEE J. Quantum Electron. **40**, 1511 (2004).
[56] Y. Hadad, J. C. Soric, A. B. Khanikaev, and A. Alù, Self-induced topological protection in nonlinear circuit arrays, Natl. Electron. Rev. **1**, 178 (2018).
[57] T. Dai, Y. Ao, J. Mao, Y. Yang, Y. Zheng, C. Zhai, Y. Li, J. Yuan, B. Tang, Z. Li, J. Luo, W. Wang, X. Hu, Q. Gong, and J. Wang, Non-Hermitian topological phase transitions controlled by nonlinearity, Nat. Phys. **20**, 101 (2024).
[58] T. Isobe, T. Yoshida, and Y. Hatsugai, Bulk-edge correspondence for nonlinear eigenvalue problems, Phys. Rev. Lett. **132**, 126601 (2024).
[59] K. Sone, M. Ezawa, Y. Ashida, N. Yoshioka, and T. Sagawa, Nonlinearity-induced topological phase transition characterized by the nonlinear Chern number, Nat. Phys. **20**, 1164 (2024).
[60] K. Sone and Y. Hatsugai, Topological-to-topological transition induced by on-site nonlinearity in a one-dimensional topological insulator, arXiv:2501.10087.
[61] L.-J. Lang, S.-L. Zhu, and Y. D. Chong, Non-Hermitian topological end breathers, Phys. Rev. B **104**, L020303 (2021).
[62] N. Pernet, P. St-Jean, D. D. Solnyshkov, G. Malpuech, N. C. Zambon, Q. Fontaine, B. Real, O. Jamadi, A. Lemaître, M. Morassi, L. L. Gratiet, T. Baptiste, A. Harouri, I. Sagnes, A. Amo, S. Ravets, and J. Bloch, Gap solitons in a one-dimensional driven-dissipative topological lattice, Nat. Phys. **18**, 678 (2022).
[63] J. Veenstra, O. Gamayun, X. Guo, A. Sarvi, C. V. Meinersen, and C. Coulais, Non-reciprocal topological solitons in active metamaterials, Nature (London) **627**, 528 (2024).
[64] M. Jürgensen, S. Mukherjee, and M. C. Rechtsman, Quantized nonlinear Thouless pumping, Nature (London) **596**, 63 (2021).
[65] Q. Fu, P. Wang, Y. V. Kartashov, V. V. Konotop, and F. Ye, Nonlinear Thouless pumping: Solitons and transport breakdown, Phys. Rev. Lett. **128**, 154101 (2022).
[66] M. Jürgensen, S. Mukherjee, C. Jörg, and M. C. Rechtsman, Quantized fractional Thouless pumping of solitons, Nat. Phys. **19**, 420 (2023).
[67] S. Ravets, N. Pernet, N. Mostaan, N. Goldman, and J. Bloch, Thouless pumping in a driven-dissipative Kerr resonator array, Phys. Rev. Lett. **134**, 093801 (2025).
[68] C. Yuce, Nonlinear non-Hermitian skin effect, Phys. Lett. A **408**, 127484 (2021).

[69] M. Ezawa, Dynamical nonlinear higher-order non-Hermitian skin effects and topological trap-skin phase, Phys. Rev. B **105**, 125421 (2022).

[70] B. Zhu, Q. Wang, D. Leykam, H. Xue, Q. J. Wang, and Y. D. Chong, Anomalous single-mode lasing induced by nonlinearity and the non-Hermitian skin effect, Phys. Rev. Lett. **129**, 013903 (2022).

[71] W. Zhang, F. Di, and X. Zhang, Non-Hermitian global synchronization, Adv. Sci. **12**, 2408460 (2025).

[72] H. Lo, Y. Wang, R. Banerjee, B. Zhang, and Y. D. Chong, Switchable non-Hermitian skin effect in Bogoliubov modes, Phys. Rev. B **111**, L241401 (2025).

[73] K. Bai, J.-Z. Li, T.-R. Liu, L. Fang, D. Wan, and M. Xiao, Nonlinear exceptional points with a complete basis in dynamics, Phys. Rev. Lett. **130**, 266901 (2023).

[74] T. Yoshida, T. Isobe, and Y. Hatsugai, Exceptional points and non-Hermitian skin effects under nonlinearity of eigenvalues, Phys. Rev. B **111**, 064310 (2025).

[75] Z.-X. Chen, Y. Ru, G.-C. He, M.-H. Lu, Y.-F. Chen, Y.-Q. Lu, and Z.-G. Chen, following Letter, Nonlinear coupling induced anomalous state transfer and complete multistate excitation via adiabatic control, Phys. Rev. Lett. **136**, 037202 (2026).